

Article

Effect of Partial Cation Replacement on Anode Performance of Sodium-Ion Batteries

Shijiang He ^{1,†}, Zidong Wang ^{2,†}, Wenbo Qiu ^{1,†}, Huaping Zhao ² and Yong Lei ^{2,*}

¹ Institute of Nanochemistry and Nanobiology, School of Environmental and Chemical Engineering, Shanghai University, Shanghai 200444, China; 21722731@shu.edu.cn (S.H.); qwb13707919802@shu.edu.cn (W.Q.)

² Fachgebiet Angewandte Nanophysik, Institut für Physik and IMN MacroNano, Technische Universität Ilmenau, 98693 Ilmenau, Germany; zidong.wang@tu-ilmenau.de (Z.W.); huaping.zhao@tu-ilmenau.de (H.Z.)

* Correspondence: yong.lei@tu-ilmenau.de

† These authors contributed equally to this work.

Abstract: Due to their high specific capacity and long cycle life, bimetallic sulfides are the preferred choice of researchers as anodes in sodium-ion batteries (SIBs). However, studies indicate that this class of materials often requires expensive elements such as Co, Sb, Sn, etc., and their performance is insufficient with the use of inexpensive Fe, V alone. Therefore, there is a need to explore the relationship between metal cations and anode performance so that the requirements of cost reduction and performance enhancement can be met simultaneously. In this work, a series of partially replaced sulfides with different cation ratios have been prepared by a hydrothermal method followed by heat treatment. By partially replacing Co in NiCo sulfides, all samples show improved capacity and stability over the original NiCo sulfides. As a result, the metal elements have different oxidation states, which leads to a higher capacity through their synergistic effects on each other. Mn-NiCoS with 10% replacement showed satisfactory capacity ($721.09 \text{ mAh g}^{-1}$ at 300 mA g^{-1} , $662.58 \text{ mAh g}^{-1}$ after 20 cycles) and excellent cycle life (85.41% capacity retention after 1000 cycles at 2000 mA g^{-1}).

Keywords: sodium-ion batteries; anode; multi-metal sulfides; partial cation replacement



Citation: He, S.; Wang, Z.; Qiu, W.; Zhao, H.; Lei, Y. Effect of Partial Cation Replacement on Anode Performance of Sodium-Ion Batteries. *Batteries* **2024**, *10*, 44. <https://doi.org/10.3390/batteries10020044>

Academic Editors: Seung-Wan Song and Hirotoshi Yamada

Received: 30 October 2023

Revised: 19 January 2024

Accepted: 24 January 2024

Published: 26 January 2024



Copyright: © 2024 by the authors. Licensee MDPI, Basel, Switzerland. This article is an open access article distributed under the terms and conditions of the Creative Commons Attribution (CC BY) license (<https://creativecommons.org/licenses/by/4.0/>).

1. Introduction

Lithium-ion batteries (LIBs), as a very mature energy storage technology, have been widely and successfully used in many applications [1,2]. Demand for LIBs also has been on the rise in recent years with the growth of the e-society [3]. However, the limited and uneven distribution of lithium resources limits the further development of LIBs [4,5]. This main reason led to sodium-ion batteries (SIBs) with similar configurations being investigated and considered as a future alternative to lithium-ion batteries. As is well known, the Stokes radius of alkali metal ions (Li^+ , Na^+ , K^+ ...) decreases with the increase in atomic number [6]. This means that the Stokes radius of sodium ions is smaller than that of lithium ions, which makes sodium ions have high ionic conductivity in low-concentration sodium salt electrolytes. This indicates that sodium ion batteries can use low-concentration sodium salt electrolytes, which has a cost advantage compared to lithium-ion batteries. In addition, the solvation ability of sodium ions is lower than that of lithium ions (about 25–30% smaller), indicating better interfacial ion diffusion ability [7–10]. However, achieving high capacity and stability in SIBs' anode materials remains challenging because sodium ions have a larger intrinsic radius than lithium ions, which may cause worse stability during charging and discharging [11]. To address this issue, various anode materials have been investigated.

Among different anode materials, the limited reversible capacity of carbon-based materials limits their widespread use, even though they are inexpensive and easily available [12,13]. Sn- and Sb-based anode materials can exhibit high sodium storage capacity (Sn can theoretically reach 847 mAh g^{-1} in sodium-ion batteries, and Sb can reach 660 mAh g^{-1}

in sodium-ion batteries). However, during the insertion/extraction process of sodium ions, they will experience severe volume expansion (420% for Sn, 390% for Sb), leading to structural collapse and rapid capacity decay [14,15]. Due to this intrinsic limitation, they are far from practical application, even though many efforts have been made. Moreover, transition metal sulfides are considered a promising choice for anode materials, due to their high capacity for multiple electron reactions, good redox activity, and smaller volume structure changes during sodium storage [16–19]. Combining these sulfides with highly conductive carbon-based materials typically increases the electrode stability performance [20–23]. However, the introduction of carbon-based materials may have negative effects, such as increasing the relative volume of the electrodes and reducing the tap density, which can affect the whole device's performance [24,25]. Further research is required to enhance the performance in such non-carbon conditions. In addition, it has been found that when a new metal element is introduced to form binary metal sulfides, there is a significant performance improvement compared to single metal sulfides [26,27]. Progress has been made in the use of binary metal sulfides as anodes for SIBs. For example, Gao et al. [28] have introduced Cr into Sb_2S_3 to form CrSbS_3 . Due to the Cr-S support, the electrodes obtained a high capacity of 544 mAh g^{-1} after 100 cycles at 0.2 A g^{-1} and maintained a capacity retention rate of 100% after 4600 cycles at 20 A g^{-1} . A $\text{FeCoS}_4@\text{carbon nanotube graphene hybrid}$ [29] exhibited smaller volume changes during repeated sodium storage/desalination processes, resulting in excellent rate performance and longer cycle life. It showed excellent cycling stability, with a stable capacity at 680 mAh g^{-1} after 1000 cycles under the current of 2.0 A g^{-1} . By [30] inducing the growth of SnCoS_4 particles on layered reduced graphene oxide (rGO), $\text{SnCoS}_4@\text{rGO}$ showed excellent sodium storage capacity, reaching a high specific capacity of 696.05 mAh g^{-1} at a current density of 0.1 A g^{-1} . Even after 1000 cycles at a current density of 5 A g^{-1} , it retained a stable capacity at 606 mAh g^{-1} . However, most of the reported binary metal sulfides contain Co, Sb, Sn, Mo, Cr, etc. These metallic elements are often characterized by an uneven distribution, small reserves, and high costs. This is inconsistent with the original aim of replacing LIBs with SIBs and therefore makes reducing costs difficult. Moreover, when more cost-effective metal elements are used, they often exhibit unsatisfactory performance, such as Fe-V sulfides [31]. This is an indication that current research is inadequate. For the economic use of the metals and to improve the performance of multi-metal sulfides, further studies are required to investigate the effect of interactions between different metal cations on anode performance [32].

Therefore, based on this idea, the most common binary transition metal sulfides, Co-Ni sulfides, were chosen as the basic object of study. Due to the similar physical and chemical properties of cobalt and nickel, binary metal sulfides in equal molar ratios are studied as a standard in this work [33]. Typically, the influence of the metal cations on anode performance was investigated by partially replacing the more crucial and expensive element, Co. After evaluating different options, manganese was selected as a viable element to replace Co. The selection fits the goal of using abundant resources in SIBs, as Mn is abundant in the earth's crust. Furthermore, the larger ionic radius of Mn ions may improve material conductivity and increase material spacing, resulting in good electrochemical performance [34–37]. Different ratios of sulfides, partially replaced with cations, were prepared while maintaining the original nanosheet structure. Additionally, a series of characterizations were used to analyze the relationship between cation ions and anode performance under partial replacement. The results showed that all partial replacements improved performance compared to the un-replaced sulfides. This can be attributed to the synergistic effect between the metal cations. Specifically, when 10% of Co was replaced with Mn, the resulting anode displayed high capacity (721.06 mAh g^{-1} at 300 mA g^{-1}) and good rate performance (583 mAh g^{-1} at 8 A g^{-1}). It also shows long-term stability, retaining 85.41% of its capacity after 1000 cycles at 2000 mA g^{-1} .

2. Materials and Methods

2.1. Materials

Nickel nitrate hexahydrate ($\text{Ni}(\text{NO}_3)_2 \cdot 6\text{H}_2\text{O}$), sodium acetate anhydrous (CH_3COONa), and sublimed sulfur (S) were purchased from Sinopharm Chemical Reagent Co., Ltd. (Shanghai, China). Cobalt nitrate hexahydrate ($\text{Co}(\text{NO}_3)_2 \cdot 6\text{H}_2\text{O}$) was purchased from Beijing Innokai Technology Co., Ltd. (Beijing, China). Polyethylene glycol (PEG-200) was purchased from Shanghai Titan Scientific Co., Ltd. (Shanghai, China). Manganese nitrate tetrahydrate ($\text{Mn}(\text{NO}_3)_2 \cdot 4\text{H}_2\text{O}$) was purchased from Aladdin Chemical Reagent Co., Ltd. (Shanghai, China). All the chemicals used in this work were of analytical grade and used as such without further purification.

2.2. Synthesis of NCS Nanosheets

Nickel-cobalt nanosheets (NCS) were prepared by a solvothermal method and following heat treatment, as shown in Figure 1. Firstly, 5 mmol $\text{Co}(\text{NO}_3)_2 \cdot 6\text{H}_2\text{O}$ (1.455 g), 5 mmol $\text{Ni}(\text{NO}_3)_2 \cdot 6\text{H}_2\text{O}$ (1.454 g), and 20 mmol NaCH_3COO (1.64 g) were added into 40 mL PEG-200, respectively. The solution was stirred at room temperature for 1.5 h until completely dissolved. The solution was then transferred into a stainless steel autoclave (80 mL) and heated at 200 °C for 16 h. After cooling to room temperature, the thin-layer structured precursor was collected and washed with deionized water and ethanol, respectively. Then, the precursors were obtained after drying at 60 °C for 12 h under vacuum. After that, sublimated sulfur and precursor (mass ratio of 4:1) were placed at each end of the boat. The sublimated sulfur was placed upstream and transferred to a tube furnace. The sample was heated at 550 °C under a 5% hydrogen-argon mixture with a heating rate of 3 °C/min for 3 h. After the tubular furnace was naturally cooled to room temperature, the obtained products were collected and named NCS.

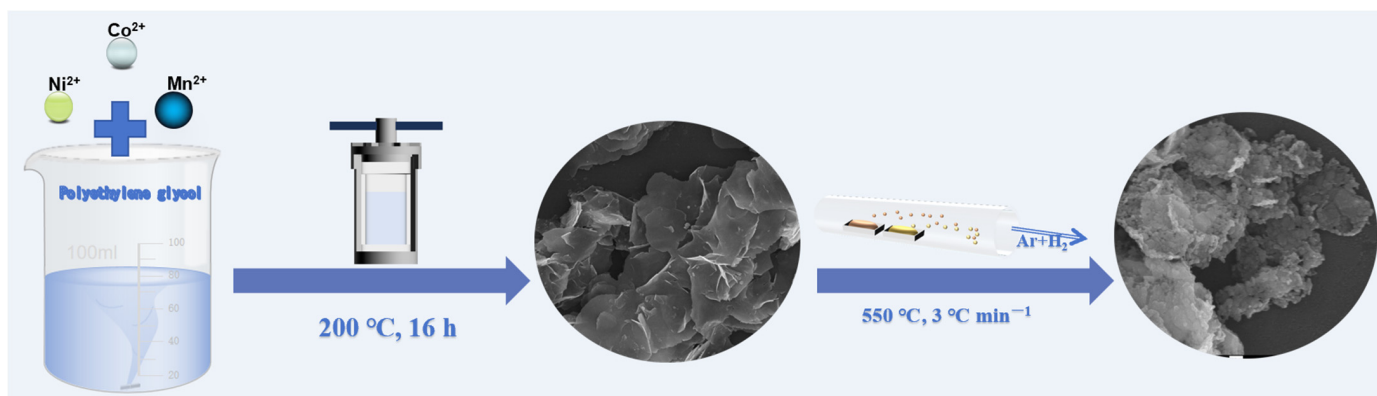


Figure 1. Schematic illustration of the basic synthesis process of NCMS.

2.3. Synthesis of Mn-Replaced NCS Nanosheets

The preparation of Mn-replaced NCS nanosheets was almost the same as that of NCS nanosheets. Different ratios of replaced NCS were obtained by adding $\text{Mn}(\text{NO}_3)_2 \cdot 4\text{H}_2\text{O}$ and adjusting the ratio of $\text{Mn}(\text{NO}_3)_2 \cdot 4\text{H}_2\text{O}$ and $\text{Co}(\text{NO}_3)_2 \cdot 6\text{H}_2\text{O}$. Equimolar amounts of $\text{Co}(\text{NO}_3)_2 \cdot 6\text{H}_2\text{O}$ were replaced with 0.25 mmol, 0.5 mmol, and 0.75 mmol of $\text{Mn}(\text{NO}_3)_2 \cdot 4\text{H}_2\text{O}$, respectively. In other words, the total molar amounts of Mn and Co remain constant. The replaced samples were named NCMS-5, NCMS-10, and NCMS-15, respectively.

3. Results and Discussion

3.1. Material Characterization

To explore the effect of Mn replacement on the morphology, the structures of samples with different replacement ratios before and after sulfidation are investigated. Uniform distributed layered nanosheets of nickel-cobalt precursor can be seen in Figure 2a. This

thin-layer structure with a thickness of about 10 nm (Figure S3) is conducive to increasing the contact area between the active material and the electrolyte and can fully expose the surface active sites. This is very helpful for accelerating mass transfer and electron transfer, which is beneficial as a pseudo capacitive anode material for high-performance sodium ion batteries. As the Mn ratio increases, the nanolayer structure of the nanosheet precursor remains unchanged compared to the Ni-Co precursor without Mn-replacement (Figure 2b–d). As shown in Figure 2e–g, sulfides all maintained the nanosheet structure of the precursors without sulfidation. High-temperature sulfidation makes the surface of the sample become rough and granular. This irregular surface provides more sites for electrochemical reactions, which may increase capacity. The detailed surface structure of samples has also been confirmed by TEM images (Figure 2i–k). From the TEM images of NCS, NCMS-5, and NCMS-10, it can be seen that the surface of the nanosheets is composed of different small nanoparticles. However, the surface of NCMS-15 is relatively smooth (Figure 2h) and also exhibits irregular holes. This expands the contact surface with the electrolyte, allowing for faster reaction kinetics [38,39]. As shown in Figure S4, NCMS-15 has thicker nanosheets compared to the other samples. Nevertheless, all the sulfides exhibit a similar nanosheet structure, indicating that the replacement by Mn retains the original structure. The difference is that when the percentage increases to 15%, the particles on the surface form larger sheets. In contrast, the surface is composed of dispersed particles at low ratios. This difference may explain the following electrochemical evaluations. The corresponding EDX images (Figure 2i) show the elemental distribution of NCMS-10. Co, Ni, Mn, and S are well distributed on the NCMS nanosheets. The uniformity of the prepared samples may also be shown.

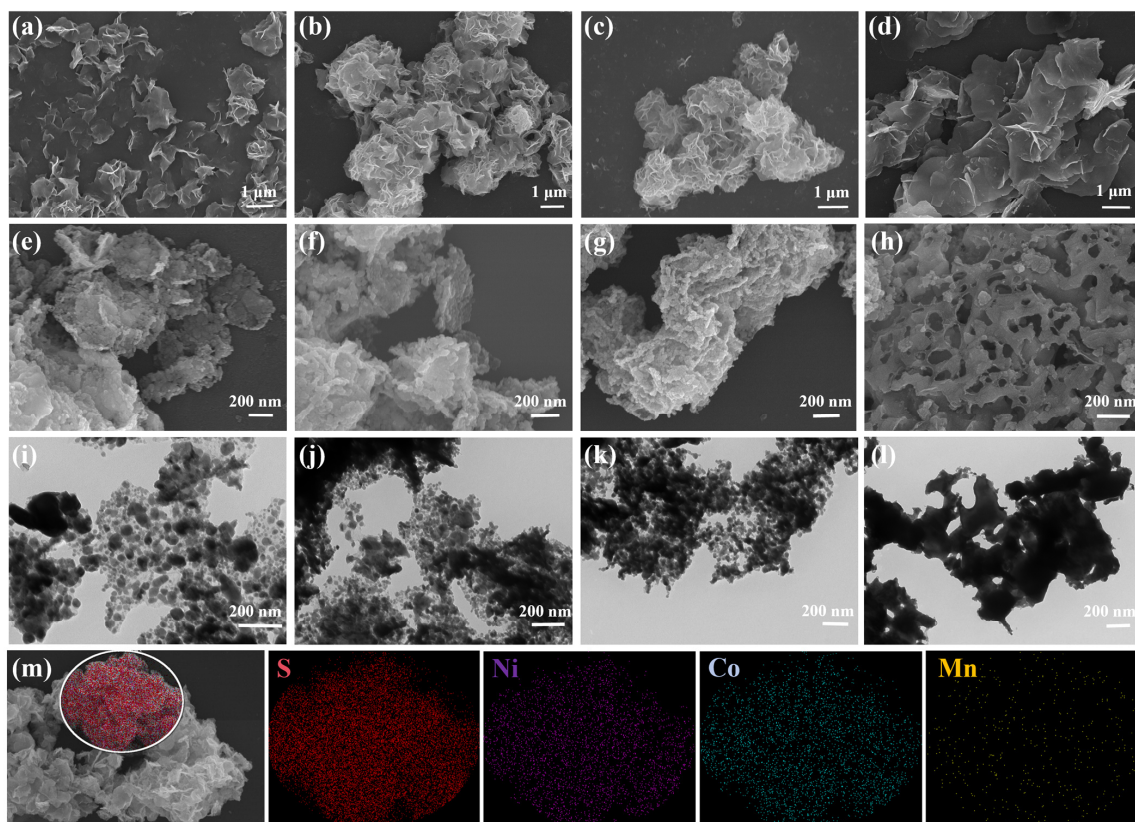


Figure 2. (a–d) SEM images of NCS, NCMS-5, NCMS-10, and NCMS-15 precursors. (e–h) SEM image of NCS, NCMS-5, NCMS-10, and NCMS-15. (i–l) TEM image of NCS, NCMS-5, NCMS-10, and NCMS-15. (m) Element mapping images of NCMS-10.

X-ray diffraction was used to identify changes in the crystal structure of the samples. Figure 3a shows the XRD patterns of Ni-Co sulfides with different replacing ratios. The patterns can be matched to the standard card (PDF 12-0723). The peaks at 15.3° , 29.6° , 31° , 47.3° , and 51.7° are attributed to the (111), (311), (222), (511), and (440) crystal planes, respectively. This indicates that Ni-Co sulfides with different replacing ratios have been successfully synthesized. It is also shown that the crystal structure remains intact despite the replacement of Co ions by Mn ions with a larger size. Because the atmosphere used for the sulfidation process contains hydrogen, part of the Ni was reduced. And the tiny characteristic peak of Ni at around 45 degrees was observed. As shown in Figure 3b, as the Mn ratio increases, the XRD diffraction peaks shift towards small angles (dashed line in Figure 3b). This is due to the larger radius of Mn compared to that of both Ni and Co atoms. A large radius reduces the diffraction angle, because the lattice spacing is negatively correlated with the diffraction angle when Co has been replaced by Mn. This facilitates the expansion of lattice volume, leading to reduced volume changes during charging and discharging.

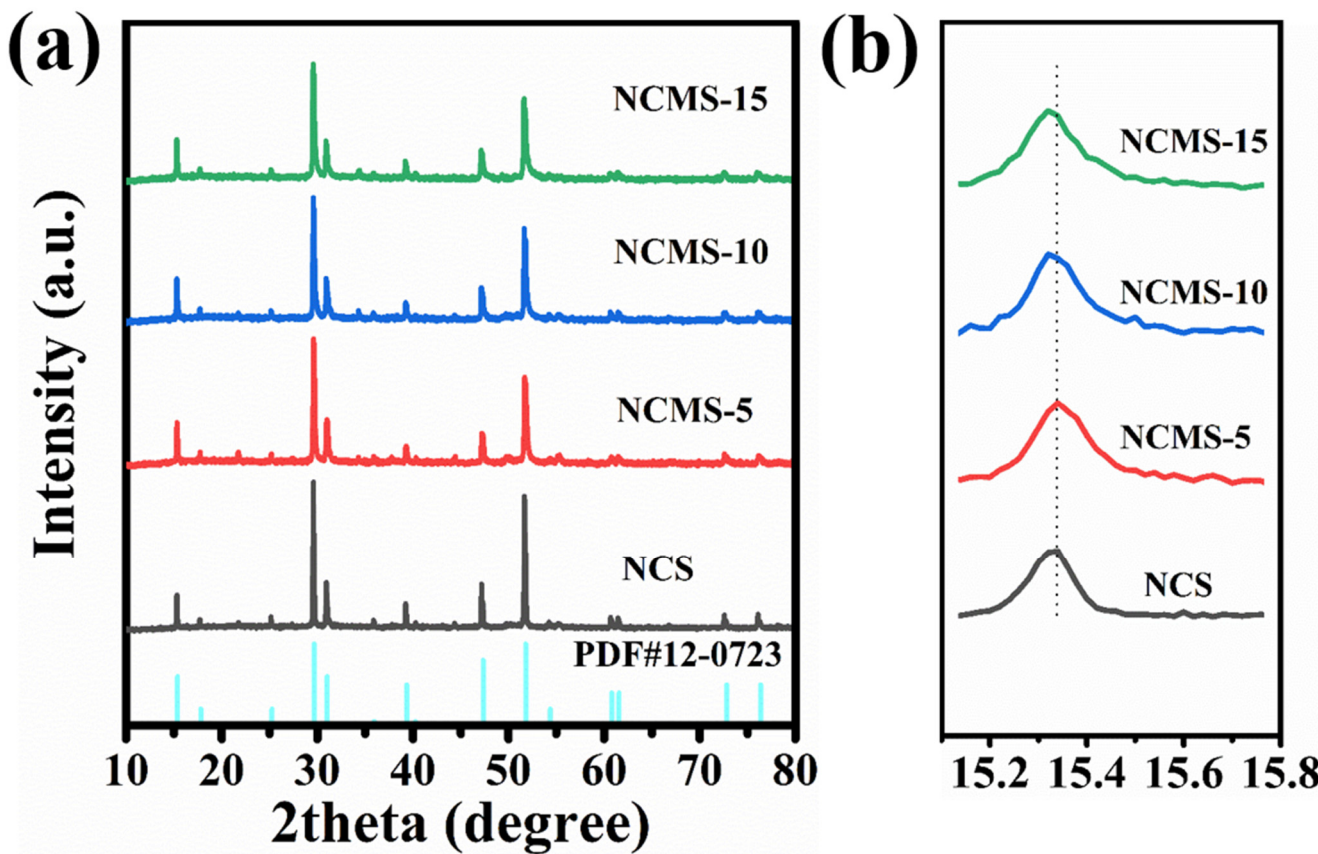


Figure 3. (a) XRD of NCS, NCMS-5, NCMS-10, and NCMS-15. (b) Magnified (111) peak of NCMS-10 samples.

XPS is used to identify changes in elemental valence, allowing for analysis of the effects of replacement on the elements. From the plots of Ni (Figure 4), all the samples exhibit a strong peak at 855.1 eV (Orange line), corresponding to Ni^{2+} . However, both NCMS-10 and NCMS-15 have another peak at 857.4 eV (Pink line), indicating the presence of Ni^{3+} . The results showed that as the replacement amount of Mn increased to 10%, Ni in the compound was present at both +2 and +3 valences, which is beneficial for high capacity during sodium storage. From the XRD test, the sample contains minor amounts of metallic nickel. However, the $\text{Ni } 2\text{p}_{3/2}$ peak position in the nickel sulfide is very close to metallic nickel. The peak located at 852.58 eV (Green line) can be related to the formation of Ni sulfide and metallic Ni [40–42]. In addition, the strong peak at 780.4 eV (Orange line) and

the satellite peak at 785.46 eV (blue line) in the Co 2p_{3/2} spectrum correspond to Co²⁺. Another peak at 778.08 eV (Green line) is related to the presence of Co³⁺, but it may also contain a small amount of metallic cobalt [43–45]. This indicates the presence of both +2 and +3 valence states of Co. In the core energy-level spectrum of Mn 2p_{3/2}, the peaks at 641.4 eV (blue line) correspond to Mn²⁺ [46]. The satellite peaks at 647.1 eV (Yellow line) are also characteristic of Mn²⁺. As the spectrum of Mn is susceptible to be influenced by other elements, there are two peaks at 644.6 eV and 638.1 eV (Orange line), which is the Ni Auger line [47,48]. For all the samples, the +2 valence state should be present. Notably, the characteristic satellite peak of Mn²⁺ in NCMS-10 indicates the presence of the +2 valence state. And the peak at 641.6 eV (Purple line) in NCMS-10 is related to the presence of Mn³⁺ [49] and may overlap with the Mn²⁺ peak. It indicated the simultaneous presence of Mn²⁺ and Mn³⁺ in NCMS-10. Moreover, the characteristic satellite peak of Mn²⁺ in NCMS-15 may be overlapped with the Auger peak of Ni. Therefore, the above XPS spectra demonstrate the presence of Mn, Co, and Ni elements in the prepared samples. These results confirm that NCMS has multivalent metal elements, which are essential for improving the electronic conductivity of nanosheets and are beneficial for the high-speed performance of sodium storage electrode materials. Moreover, in the S 2p (Figure S1b) spectrometer, four sets of characteristic peaks of S²⁻ can be obtained within the range of 160~166 eV. The two peaks centered around 160.78 and 162.01 eV belong to the 2p_{3/2} of S²⁻, and the other two peaks belong to the 2p_{1/2} characteristic.

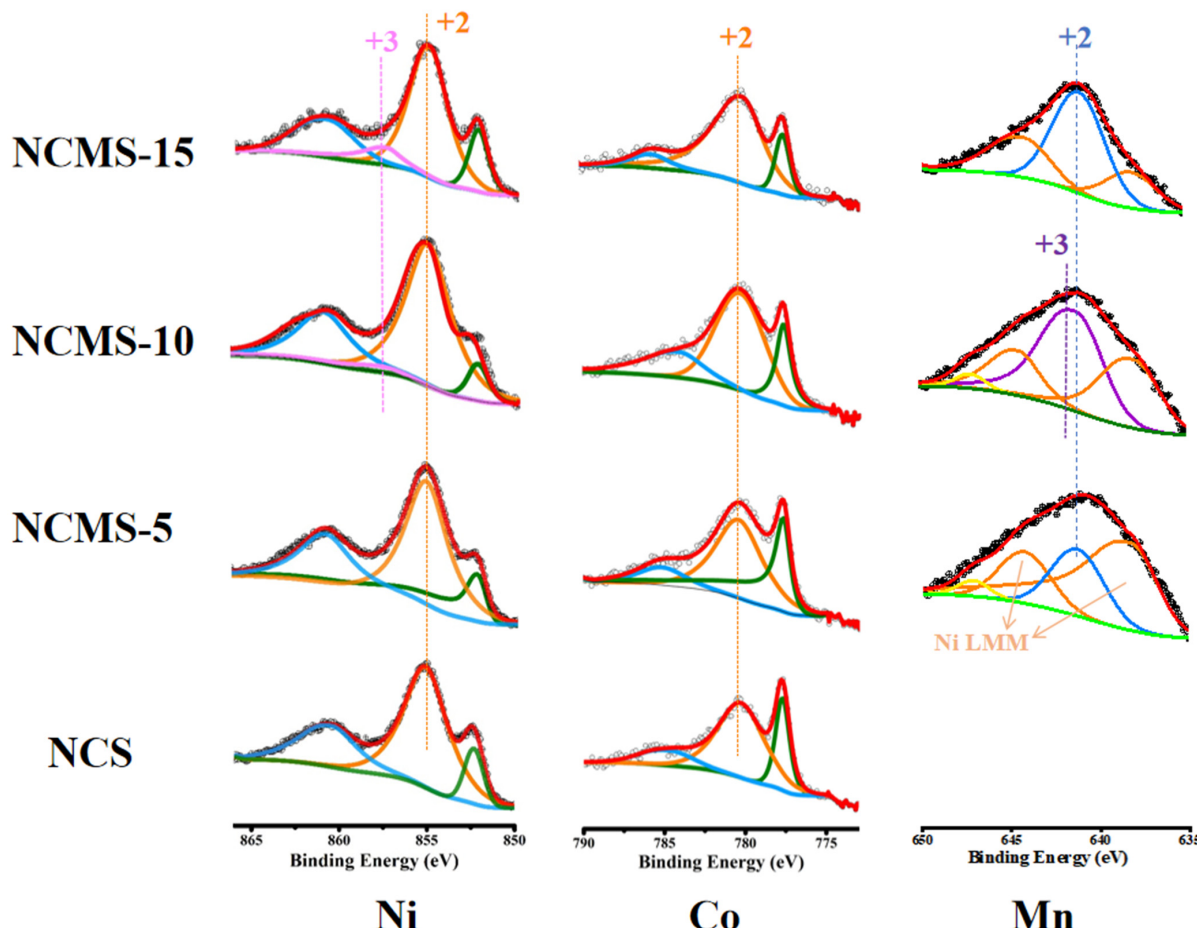


Figure 4. High-resolution XPS spectra of Ni 2p, Co 2p, and Mn 2p of NCS, NCMS-5, NCMS-10, and NCMS-15, respectively. Scattered dots represent the raw scan counts of XPS spectra, red lines represent the fitted counts of XPS, and dashed lines represent the peak positions of different valences.

3.2. Electrochemical Performance

Cyclic voltammetry (CV) was used to determine the reactions during the charging and discharging of the electrodes. To further investigate the partial replacement, the curves of NCMS-10 with different cycles have been displayed in Figure 5a. A strong peak at 0.69 V during the first cathode scan corresponded to the formation of a solid electrolyte interface (SEI) and the conversion reaction related to sodium storage in NCMS-10 nanosheets. During anodic scanning, there is a clear peak at around 1.685 V, corresponding to the reaction of sodium removal on the surface of the electrode material. During the second charging and discharging process, three distinct peaks appeared at 1.35 V, 0.58 V, and 0.23 V. The first two peaks were related to the formation of NiS_2 , CoS_2 , and Na_2S . The peak at 0.23 V represents the subsequent conversion reaction, indicating that NCMS-10 undergoes multi-step electrochemical reactions. From Figure S4, it can be seen that except for NCS, all other samples have a peak near 0.2 V. This indicates that the introduction of Mn enhances the electrochemical reaction during the charging and discharging process, thereby increasing the capacity. Meanwhile, a large radius of Mn could damage the structural stability of the electrode material, resulting in decreased stability. However, from the second scan, it is indicated that NCMS-10 possesses high reversibility and stability during repeated charging and discharging, as the CV curves nearly overlap. Figure 5b shows the charging/discharging curves of NCMS-10 under different cycles at a current density of 0.3 A g^{-1} . In the first cycle, a high discharge specific capacity of $721.09 \text{ mAh g}^{-1}$ can be obtained, with an initial Coulombic efficiency of 97.98%. This high initial Coulombic efficiency can be attributed to the large amount of Na^+ stored in different electrochemical conversion reactions that occur in the initial stage. The discharge capacity for the 5th, 10th, 15th, and 20th cycles of NCMS-10 is 649.7, 634.4, 646.5, and 662.6 mAh g^{-1} , respectively. This indicates that the prepared sample exhibits high-capacity performance when used as an anode material for sodium-ion batteries. In addition, similar curves at different cycles also indicate the stability of the material. As shown in Figure S5, the introduction of Mn enhances the capacity of the samples. Rate performance is demonstrated to evaluate the effects of different replacement ratios. As shown in Figure 5c, significant improvements in the rate performance can be observed for the original samples after replacement. The capacity of the material gradually increases as the replacement percentage increases. The results indicate that the replacement strategy effectively increased the capacity of the original bimetallic sulfide, but a suitable ratio is still required to enhance the rate performance associated with the increased capacity. Among them, NCMS-10 performs better in the high current density, exhibiting a more stable rate performance. The NCMS-10 electrode displayed a good reversible specific capacity at different current rates ranging from 0.3 A g^{-1} to 8 A g^{-1} , with capacities of 686.6, 623.7, 616.2, 604.6, 595.7, 595.1, 593.8, and 583 mAh g^{-1} , respectively. The electrode capacity also returned to 672.1 mAh g^{-1} when the current density was returned to 0.3 A g^{-1} . The higher capacity performance can be attributed to electrode activation at different current densities. The reasons for the improved performance were analyzed using a Nyquist plot in the frequency range of 0.01 to 100 kHz. To better explain the Nyquist diagram, we have inserted an equivalent circuit in Figure 5d. It includes the internal impedance (R_s) of the battery, the charge transfer resistance (R_{ct}) at the interface between the electrode and the electrolyte, the impedance of the double-layer capacitor (CPE), and the Warburg factor (Z_w) of the ion diffusion resistance. The Nyquist diagram can be roughly divided into two parts, a semicircle and a line, where the semicircle represents the interfacial transfer resistance of sodium ions. The smaller the diameter of the semicircle, the lower the resistance, which is more conducive to charge transfer. Figure 5d provides a comparison chart after 20 cycles. Compared with NCS, the R_{ct} of NCMS-10 decreased from 30.45Ω to 4.034Ω after being replaced by Mn, which is also lower than that of NCMS-5 and NCMS-15 nanosheets (7.803 and 8.675Ω), indicating that NCMS-10 has better chemical reaction kinetics. In addition, compared to the Nyquist plot of NCMS-10 with 0 cycles (Figure 5e), the semicircle (R_{ct}) after 20 cycles can be ignored. Compared to NCS, the R_{ct} of NCMS-10 is only 4.034Ω , which is lower than that of NCMS-5 and NCMS-15 (7.803 and 8.675Ω).

The replaced NCS has the highest R_{ct} of $30.45\ \Omega$, which is larger than all the replaced materials. The data indicate that replacement can effectively improve the chemical reaction kinetics performance, and NCMS-10 has better performance. In addition, compared to the Nyquist plot of NCMS-10 with 0 cycles, the semicircle (R_{ct}) after 20 cycles can be ignored, corresponding to the good stability described above. Hence, appropriate substitution of atoms can increase the active sites of electrochemical reactions, increase crystal defects, accelerate the transport of sodium ions, and improve rate performance. As shown in Figure 5f, NCMS-10 exhibits superior rate performance compared to recently reported transition metal sulfide materials. The advantages of this partial replacement strategy are further demonstrated. The cycling performance of samples with different replacement ratios at a rate of $2\ \text{A g}^{-1}$ is shown in Figure 5g. As shown in the curves, the NCMS-10 exhibits both high capacity and considerable stability, maintaining 85.41% of its capacity after 300 cycles. It is also observed that the performance is better than the original samples, regardless of the percentage of replacement. The results show that replacement can improve performance through the synergistic effect of metal ions. To further demonstrate the superiority of the NCMS-10, more cycles have been tested at a high current density of $2\ \text{A g}^{-1}$. As shown in Figure 5h, it can achieve a high capacity of $621.9\ \text{mAh g}^{-1}$ after 1000 cycles, maintaining 73.2% of its capacity. Although there was a noticeable decrease in capacity during the initial 30 cycles (from $751.3\ \text{mAh g}^{-1}$ to $648.8\ \text{mAh g}^{-1}$), it remained relatively consistent during the following cycles.

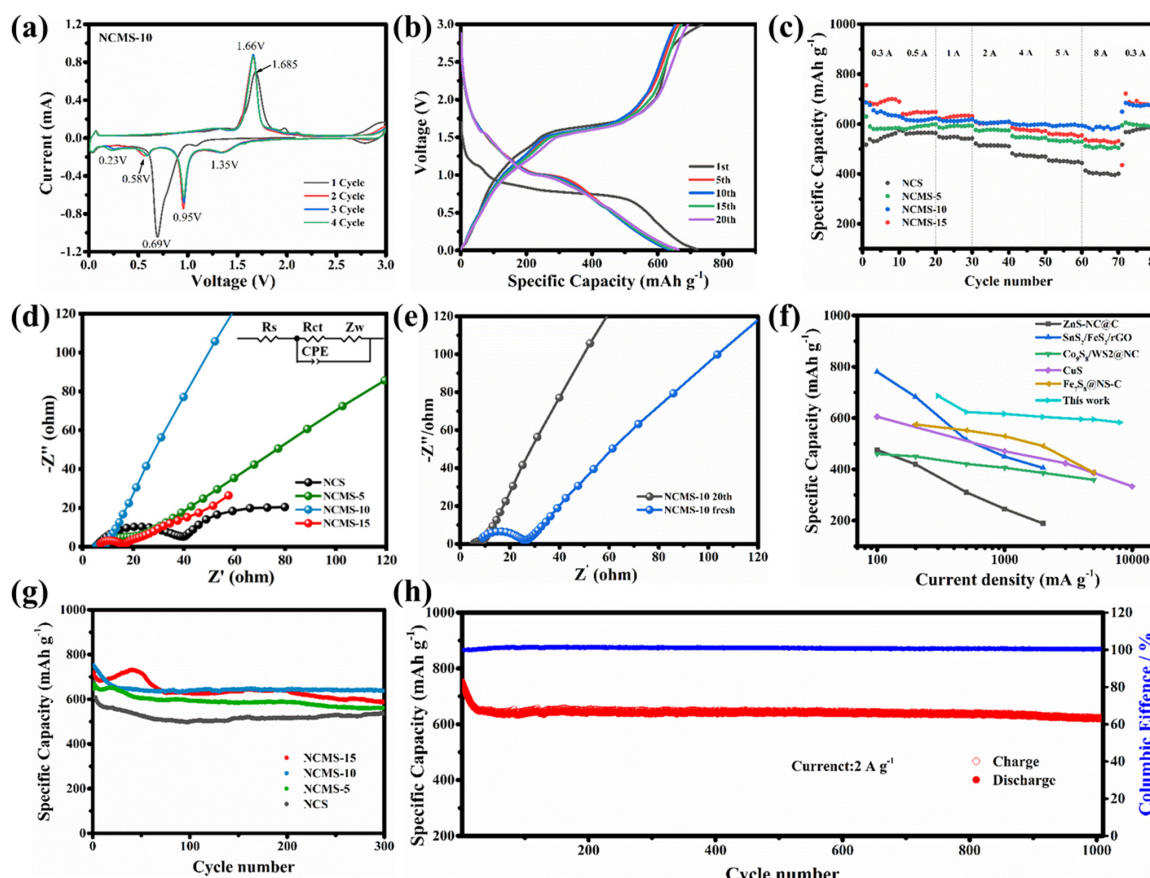


Figure 5. (a) CV curves of NCMS-10 at $0.1\ \text{mV s}^{-1}$. (b) Charge/discharge profiles at different cycles of NCMS-10 at $0.3\ \text{A g}^{-1}$. (c) Rate performance of NCS, NCMS-5, NCMS-10, and NCMS-15 from 0.3 to $8.0\ \text{A g}^{-1}$. Nyquist plots of (d) different electrodes after 20 cycles at $0.3\ \text{A g}^{-1}$, respectively, and (e) NCMS-10 before and after 20 cycles. (f) Comparison of rate performance between NCMS-10 and previously reported materials. (g) Comparison of cycling performance of different electrodes at $2\ \text{A g}^{-1}$. (h) Cycle performance of NCMS-10 at $2\ \text{A g}^{-1}$.

To further investigate the effect of partial replacement on anode performance, CV curves with different scan rates ($0.1\text{--}0.8\text{ mV s}^{-1}$) were tested for different replaced samples (Figure 6a). It can be seen that all the peak currents of the CV curves increase as the scan rates increase. They all show similar shapes during different scan rates, indicating good rate performance and charge transfer kinetic processes. Faraday and surface capacitive contributions to charge storage can be distinguished using Equation (1):

$$i = a v^b, \quad (1)$$

where i and v represent the peak current and scanning rate, respectively. For better understanding, Equation (2) is shown, derived from Equation (1):

$$\log(i) = b \log(v) + \log(a), \quad (2)$$

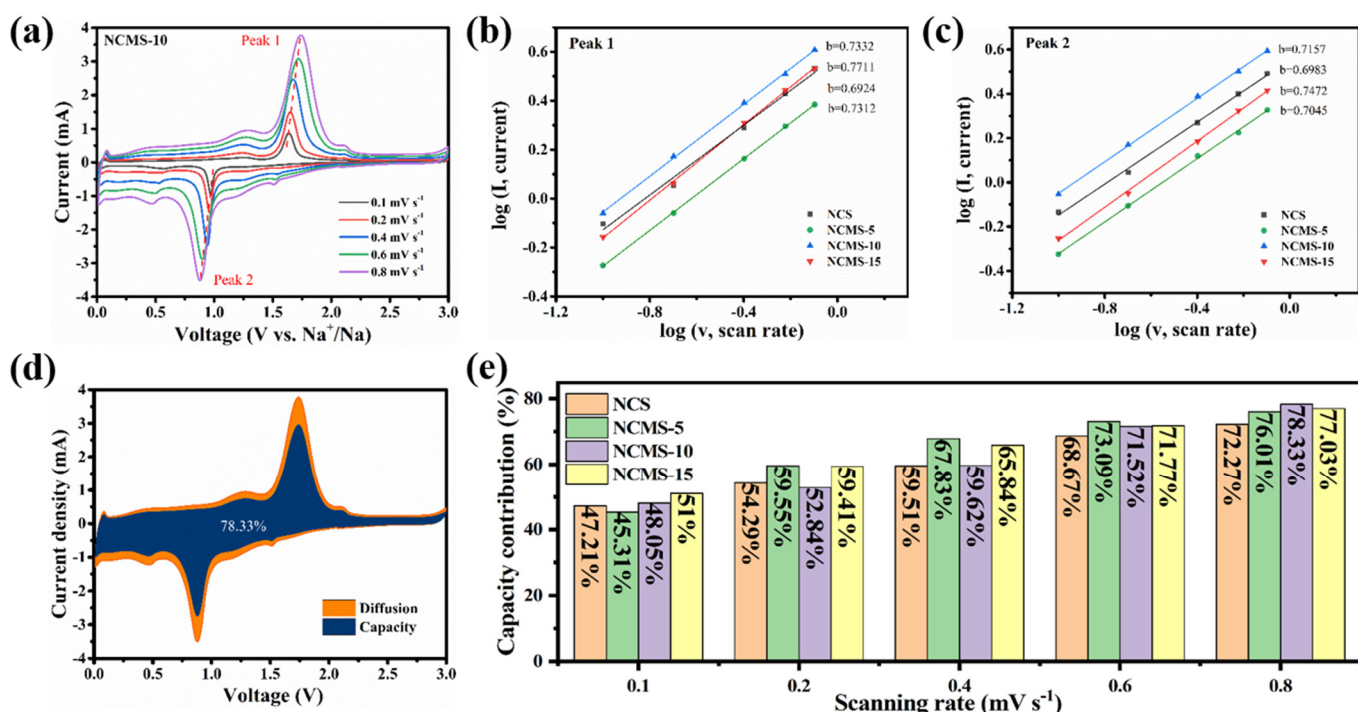


Figure 6. (a) CV curves of NCMS-10 at various scanning rates. The relationship of the log (scan rate) and log (peak current) for (b) peak 1 and (c) peak 2. (d) Capacitive contribution of NCMS-10 at 0.8 mV s^{-1} . (e) Capacity contribution at different scanning rates of NCS, NCMS-5, NCMS-10, and NCMS-15 electrodes, respectively.

Among them, a and b are two controllable parameters: a is a constant, and b can be determined by corresponding $\log(i)$ and $\log(v)$ in Equation (2). Usually, the value range of b is $0.5\text{--}1$, indicating mixed control behavior. A value close to 1 indicates the dominance of capacitive electrochemical behavior, whereas a b value close to 0.5 indicates the dominance of diffusion-controlled electrochemical behavior [50]. Figure 6b,c shows the b values of different redox peaks calculated using the above formula. The b values of the oxidation and reduction peaks of NCMS-10 are 0.7332 and 0.7157, respectively, which are greater than the b values corresponding to the oxidation and reduction peaks of NCS (0.6924 and 0.6983), indicating that faster capacitors control the charging and discharging process of NCMS-10.

To further investigate the contribution of the capacitive process at different rates, the following Equation (3) has been used:

$$i = k_1 v + k_2 v^{1/2}, \quad (3)$$

where $k_1 v$ represents the contribution of capacitive behavior, and $k_2 v^{1/2}$ represents the contribution of ion diffusion. Figure 6d,e shows the capacitive contribution of NCMS-10 at different scanning rates. It can be seen that as the scanning speed increases, the contribution rate of pseudo capacitance also increases. Finally, when scanned at 0.8 mV, NCMS-10 reaches a contribution of 78.33%, which is higher than that of NCS, NCMS-5, and NCMS-15 (72.27%, 76.01%, and 77.03%) at the same scanning rate. This indicates that it has better charge transfer kinetics. It should be noted that though the capacitive contribution of NCMS-10 is not the highest at a low scanning rate (0.1 mV s^{-1}), it increases more rapidly at high scanning rates. This indicates that NCMS-10 has faster kinetics at high current densities, enabling it to charge and discharge quickly in a short duration.

4. Conclusions

Briefly, a series of sulfides with different metal ratios were prepared by partially replacing metal cations with Mn in the original sulfides. The replaced samples demonstrated improved performance compared to the initial materials. This enhancement can be ascribed to the improved reaction kinetics and sodium ion storage capacity by the introduction of Mn. Meanwhile, the unique structure can reduce volume expansion and improve stability. In addition, the irregular surface provides full access to the electrolyte, exposing more active sites to improve conductivity and rate performance. As a SIB anode, NCMS-10 exhibits relatively high reversible specific capacity (662.58 mA g^{-1} at 0.3 A g^{-1}), excellent rate performance (583 mAh g^{-1} at 8 A g^{-1}), and ultra-long cycle performance (621.9 mAh g^{-1} after 1000 cycles). These results provide important insights and evidence that the addition of appropriate amounts of metal atoms can lead to the favorable transformation of bimetallic sulfides. When used as a SIB anode, it can exhibit high-rate performance and long cycle life regardless of the potential conversion mechanism of electrochemical reactions.

Supplementary Materials: The following supporting information can be downloaded at: <https://www.mdpi.com/article/10.3390/batteries10020044/s1>, Instrumentation and Sample Analysis; Electrochemical measurement; Figure S1: XPS full spectra of NCMS-10 sample. (a) Survey spectrum, (b) S 2p; Figure S2: (a–d) TEM images of NCS, NCMS-5, NCMS-10, and NCMS-15 precursors, respectively; Figure S3: SEM images of Ni-Co precursor without Mn addition.; Figure S4: CV curves of (a) NCS, (b) NCMS-5, and (c) NCMS-15 at 0.1 mV s^{-1} ; Figure S5: Charge/discharge profiles at different cycles of (a) NCS, (b) NCMS-5, and (c) NCMS-15 at 0.3 A g^{-1} ; Figure S6: CV curves of (a) NCS, (b) NCMS-5, and (c) NCMS-15 at different scanning rates, respectively; Table S1: Performance comparison between this work and existing studies. References [51–55] are cited in the supplementary materials.

Author Contributions: Conceptualization, S.H. and Z.W.; methodology, S.H.; software, S.H. and W.Q.; validation, S.H., W.Q. and Z.W.; formal analysis, S.H. and Z.W.; investigation, W.Q. and Z.W.; resources, S.H.; data curation, S.H. and H.Z.; writing—original draft preparation, S.H. and Z.W.; writing—review and editing, S.H., Z.W. and H.Z.; visualization, S.H. and Z.W.; supervision, Y.L.; project administration, Y.L.; funding acquisition, Y.L. All authors have read and agreed to the published version of the manuscript.

Funding: This research was funded by the German Research Foundation (DFG: LE 2249/15-1), the Sino-German Center for Research Promotion (GZ1579), and the National Natural Science Foundation of China (22076116). Zidong Wang would like to acknowledge the support from the China Scholarship Council (No. 202007030003).

Data Availability Statement: The data that support the findings of this study are available from the corresponding author upon reasonable request.

Conflicts of Interest: The authors declare no conflicts of interest.

References

- Shang, C.; Li, X.L.; Wei, R.; Liu, X.Q.; Xu, S.Q.; Zhang, J.J. Research progress of metal oxide glass anode materials for lithium-ion batteries: A Review. *J. Non. Cryst. Solids* **2023**, *618*, 122547. [[CrossRef](#)]
- Majid, S.; Ali, A.S.G.; Taieb, S.; Mehran, A.G.; Asim, M.; Shayan, J.; Reza, R.; Meng, X.M.; Jin, Z.; Ge, Q. A Review of Nitrogen-Doped Carbon Materials for Lithium-Ion Battery Anodes. *Carbon* **2023**, *209*, 247–278. [[CrossRef](#)]
- Maia, B.A.; Magalhaes, N.; Cunha, E.; Braga, M.H.; Santos, R.M.; Correia, N. Designing Versatile Polymers for Lithium-Ion Battery Applications: A Review. *Polymers* **2022**, *14*, 403. [[CrossRef](#)] [[PubMed](#)]
- Liu, C.B.; Sun, J.C.; Zheng, P.L.; Jiang, L.; Liu, H.Y.; Chai, J.C.; Liu, Q.Y.; Liu, Z.H.; Zheng, Y.; Rui, X.H. Recent advances of non-lithium metal anode materials for solid-state lithium-ion batteries. *J. Mater. Chem. A* **2022**, *10*, 16761–16778. [[CrossRef](#)]
- Zhu, S.Y.; Li, H.Y.; Hu, Z.L.; Zhang, Q.B.; Zhao, J.B.; Zhang, L. Research Progresses on Structural Optimization and Interfacial Modification of Silicon Monoxide Anode for Lithium-Ion Battery. *Acta Phys. Chim. Sin.* **2022**, *38*, 210305. [[CrossRef](#)]
- Hayamizu, K.; Chiba, Y.; Haishi, T. Dynamic ionic radius of alkali metal ions in aqueous solution: A pulsed-field gradient NMR study. *Rsc Adv.* **2021**, *11*, 20252–20257. [[CrossRef](#)]
- Tian, Z.N.; Zou, Y.G.; Liu, G.; Wang, Y.Z.; Yin, J.; Ming, J.; Alshareef, H.N. Electrolyte Solvation Structure Design for Sodium Ion Batteries. *Adv. Sci.* **2022**, *9*, 2201207. [[CrossRef](#)]
- Lu, B.; Lin, C.J.; Xiong, H.J.; Zhang, C.; Fang, L.; Sun, J.Z.; Hu, Z.H.; Wu, Y.L.; Fan, X.H.; Li, G.F.; et al. Hard-Carbon Negative Electrodes from Biomasses for Sodium-Ion Batteries. *Molecules* **2023**, *28*, 4027. [[CrossRef](#)]
- Bai, X.; Wu, N.N.; Yu, G.C.; Li, T. Recent Advances in Anode Materials for Sodium-Ion Batteries. *Inorganics* **2023**, *11*, 289. [[CrossRef](#)]
- Xu, Z.; Wang, J.; Guo, Z.Y.; Xie, F.; Liu, H.Y.; Yadegari, H.; Tebyetekerwa, M.; Ryan, M.P.; Hu, Y.S.; Titirici, M.M. The Role of Hydrothermal Carbonization in Sustainable Sodium-Ion Battery Anodes. *Adv. Energy Mater.* **2022**, *12*, 2200208. [[CrossRef](#)]
- dos Reis, G.S.; Molaiyan, P.; Subramaniyam, C.M.; García-Alvarado, F.; Paoletta, A.; de Oliveira, H.P.; Lassi, U. Biomass-derived carbon-silicon composites (C@Si) as anodes for lithium-ion and sodium-ion batteries: A promising strategy towards long-term cycling stability: A mini review. *Electrochim. Commun.* **2023**, *153*, 107536. [[CrossRef](#)]
- Jaberi, S.Y.S.; Ghaffarinejad, A.; Khajehsaeidi, Z.; Sadeghi, A. The synthesis, properties, and potential applications of CoS₂ as a transition metal dichalcogenide (TMD). *Int. J. Hydrogen Energy* **2023**, *48*, 15831–15878. [[CrossRef](#)]
- Yin, Z.; Hu, M.; Liu, J.; Fu, H.; Wang, Z.J.; Tang, A.W. Tunable crystal structure of Cu-Zn-Sn-S nanocrystals for improving photocatalytic hydrogen evolution enabled by copper element regulation. *J. Semicond.* **2022**, *43*, 032701. [[CrossRef](#)]
- Ying, H.J.; Han, W.Q. Metallic Sn-Based Anode Materials: Application in High-Performance Lithium-Ion and Sodium-Ion Batteries. *Adv. Sci.* **2017**, *4*, 1700298. [[CrossRef](#)]
- Zheng, X.M.; You, J.H.; Fan, J.J.; Tu, G.P.; Rong, W.Q.; Li, W.J.; Wang, Y.X.; Tao, S.; Zhang, P.Y.; Zhang, S.Y.; et al. Electrodeposited binder-free Sb/NiSb anode of sodium-ion batteries with excellent cycle stability and rate capability and new insights into its reaction mechanism by operando XRD analysis. *Nano Energy* **2020**, *77*, 105123. [[CrossRef](#)]
- Wang, Z.D.; Hong, P.; Zhao, H.P.; Lei, Y. Recent Developments and Future Prospects of Transition Metal Compounds as Electrode Materials for Potassium-Ion Hybrid Capacitors. *Adv. Mater. Technol.* **2023**, *8*, 2200515. [[CrossRef](#)]
- Li, Z.W.; Yang, Y.X.; Wen, B.; Liu, X.F.; Wang, Y.J.; Du, F.; Ma, M.M.; Li, L.; Yang, G.R.; Ding, S.J. Recovered cobalt-nickel sulfide from spent lithium-ion batteries as an advanced anode material toward sodium-ion batteries. *J. Alloys Compd.* **2023**, *956*, 170328. [[CrossRef](#)]
- Wu, Y.H.; Chen, G.B.; Wu, X.A.; Li, L.; Yue, J.Y.; Guan, Y.Y.; Hou, J.; Shi, F.N.; Liang, J.Y. Research progress on vanadium oxides for potassium-ion batteries. *J. Semicond.* **2023**, *44*, 041701. [[CrossRef](#)]
- Yin, H.; Jia, L.; Li, H.Y.; Liu, A.; Li, G.Y.; Zhu, Y.C.; Huang, J.L.; Cao, M.L.; Hou, Z.H. Point-cavity-like carbon layer coated SnS nanotubes with improved energy storage capacity for lithium/sodium ion batteries. *J. Energy Storage* **2023**, *65*, 107354. [[CrossRef](#)]
- Peng, B.; Liu, X.; Cui, Z.N.; Wang, Y.D.; Zhu, T.; Tan, Z.Q.; Li, M.F.; Wang, D. MOF-derived Ni₃S₂@C grown in situ on modified cotton textile as self-standing electrodes towards high performance sodium ion batteries. *J. Alloys Compd.* **2023**, *967*, 171743. [[CrossRef](#)]
- Yang, K.; Fu, H.; Duan, Y.X.; Wang, M.X.; Tran, M.X.; Lee, J.K.; Yang, W.; Liu, G.C. Uniform Metal Sulfide@N-doped Carbon Nanospheres for Sodium Storage: Universal Synthesis Strategy and Superior Performance. *Energy Environ. Mater.* **2023**, *6*, e12380. [[CrossRef](#)]
- Chao, X.; Yan, C.Z.; Zhao, H.P.; Wang, Z.J.; Lei, Y. Micro-nano structural electrode architecture for high power energy storage. *J. Semicond.* **2023**, *44*, 050201. [[CrossRef](#)]
- Hu, P.; Dong, Y.L.; Yang, G.W.; Chao, X.; He, S.J.; Zhao, H.P.; Fu, Q.; Lei, Y. Hollow CuSbSy Coated by Nitrogen-Doped Carbon as Anode Electrode for High-Performance Potassium-Ion Storage. *Batteries* **2023**, *9*, 238. [[CrossRef](#)]
- Dong, Y.L.; Xu, C.F.; Li, Y.L.; Zhang, C.L.; Zhao, H.P.; Kaiser, U.; Lei, Y. Ultrahigh-Rate and Ultralong-Duration Sodium Storage Enabled by Sodiation-Driven Reconfiguration. *Adv. Energy Mater.* **2023**, *13*, 2204324. [[CrossRef](#)]
- Li, C.W.; Hou, J.C.; Zhang, J.Y.; Li, X.Y.; Jiang, S.Q.; Zhang, G.Q.; Yao, Z.J.; Liu, T.C.; Shen, S.H.; Liu, Z.Q.; et al. Heterostructured NiS@SnS hollow spheres as superior high-rate and durable anodes for sodium-ion batteries. *Sci. China Chem.* **2022**, *65*, 1420–1432. [[CrossRef](#)]

26. Sun, G.; Lin, H.Z.; Tian, R.Y.; Wei, Z.X.; Wang, X.Q.; Jin, X.; Yao, S.Y.; Chen, G.; Shen, Z.X.; Du, F. Rational design and synthesis of nanosheets self-assembled hierarchical flower-ball-like CuFeS for boosted wide temperature sodium-ion batteries. *Nano Res.* **2023**, *16*, 9407–9415. [[CrossRef](#)]
27. He, S.J.; Wang, Z.D.; Wang, Z.J.; Lei, Y. Recent progress and future prospect of novel multi-ion storage devices. *J. Semicond.* **2023**, *44*, 040201. [[CrossRef](#)]
28. Gao, Y.S.; Peng, B.X.; Lv, Z.R.; Han, Z.; Hu, K.Y.; Huang, F.Q. Bifunctional structure modulation of Sb-based sulfide for boosting fast and high-capacity sodium storage. *Inorg. Chem. Front.* **2023**, *10*, 2466–2473. [[CrossRef](#)]
29. Hao, Z.Q.; Dimov, N.; Chang, J.K.; Okada, S. Synthesis of bimetallic sulfide FeCoS@carbon nanotube graphene hybrid as a high-performance anode material for sodium-ion batteries. *Chem. Eng. J.* **2021**, *423*, 130070. [[CrossRef](#)]
30. Zhang, Y.X.; Jin, Y.H.; Song, Y.Y.; Wang, H.; Jia, M.Q. Induced bimetallic sulfide growth with reduced graphene oxide for high-performance sodium storage. *J. Colloid Interface Sci.* **2023**, *642*, 554–564. [[CrossRef](#)]
31. Krengel, M.; Adelhelm, P.; Klein, F.; Bensch, W. FeVS as a high-capacity electrode material for sodium-ion batteries. *Chem. Commun.* **2015**, *51*, 13500–13503. [[CrossRef](#)] [[PubMed](#)]
32. Zhao, J.; Zhang, Y.; Chen, X.; Sun, G.; Yang, X.; Zeng, Y.; Tian, R.Y.; Du, F. Entropy-Change Driven Highly Reversible Sodium Storage for Conversion-Type Sulfide. *Adv. Funct. Mater.* **2022**, *32*, 2206531. [[CrossRef](#)]
33. Zhang, X.M.; Zhao, Q.H.; Ma, T.H.; Li, Z.Q.; Tan, X.F.; Bateer, B. Design of thin-layer porous nickel cobalt sulfide for high-performance asymmetric supercapacitors. *J. Alloys Compd.* **2023**, *945*, 168902. [[CrossRef](#)]
34. Wang, K.; Zhuo, H.X.; Wang, J.T.; Poon, F.; Sun, X.L.; Xiao, B.W. Recent Advances in Mn-Rich Layered Materials for Sodium-Ion Batteries. *Adv. Funct. Mater.* **2023**, *33*, 2212607. [[CrossRef](#)]
35. Ma, J.Y.; Guo, E.Y.; Yin, L.W. Porous hierarchical spinel Mn-doped NiCoO nanosheet architectures as high-performance anodes for lithium-ion batteries and electrochemical reaction mechanism. *J. Mater. Sci. Mater. Electron.* **2019**, *30*, 8555–8567. [[CrossRef](#)]
36. Chen, H.Y.; Yang, X.T.; Lv, P.F.; Tian, P.F.; Wan, S.Y.; Liu, Q.M. Mn-doped FeS with larger lattice spacing as advance anode for sodium ion half/full battery. *Chem. Eng. J.* **2022**, *450*, 137960. [[CrossRef](#)]
37. Meng, X.R.; Chai, C.C.; Li, F.X.; Sun, Y.; Yang, Y.T. High-power microwaves response characteristics of silicon and GaAs solar cells. *J. Semicond.* **2022**, *43*, 112701. [[CrossRef](#)]
38. Chen, Y.; Fan, Z.X.; Zhang, Z.C.; Niu, W.X.; Li, C.L.; Yang, N.L.; Chen, B.; Zhang, H. Two-Dimensional Metal Nanomaterials: Synthesis, Properties, and Applications. *Chem. Rev.* **2018**, *118*, 6409–6455. [[CrossRef](#)] [[PubMed](#)]
39. Mao, L.; Zhao, X.; Wang, H.Y.; Xu, H.; Xie, L.; Zhao, C.L.; Chen, L.Y. Novel Two-dimensional Porous Materials for Electrochemical Energy Storage: A Minireview. *Chem. Rec.* **2020**, *20*, 922–935. [[CrossRef](#)]
40. Jiang, N.; Tang, Q.; Sheng, M.L.; You, B.; Jiang, D.E.; Sun, Y.J. Nickel sulfides for electrocatalytic hydrogen evolution under alkaline conditions: A case study of crystalline NiS, Ni₃S₂, and NiS nanoparticles. *Catal. Sci. Technol.* **2016**, *6*, 1077–1084. [[CrossRef](#)]
41. Nesbitt, H.W.; Legrand, D.; Bancroft, G.M. Interpretation of Ni 2p XPS spectra of Ni conductors and Ni insulators. *Phys. Chem. Miner.* **2000**, *27*, 357–366. [[CrossRef](#)]
42. Zhang, Y.L.; Wei, S.Q.; Xing, P.X.; Dai, L.Y.; Wang, Y.Y. Iron-doped nickel sulfide nanoparticles grown on N-doped reduced graphene oxide as efficient electrocatalysts for oxygen evolution reaction. *J. Electroanal. Chem.* **2023**, *936*, 117323. [[CrossRef](#)]
43. Zhao, W.W.; Bothra, P.; Lu, Z.Y.; Li, Y.B.; Mei, L.P.; Liu, K.; Zhao, Z.H.; Chen, G.X.; Back, S.; Siahrostami, S.; et al. Improved Oxygen Reduction Reaction Activity of Nanostructured CoS through Electrochemical Tuning. *ACS Appl. Energy Mater.* **2019**, *2*, 8605–8614. [[CrossRef](#)]
44. Zhang, J.Y.; Xiao, W.; Xi, P.X.; Xi, S.B.; Du, Y.H.; Gao, D.Q.; Ding, J. Activating and Optimizing Activity of CoS for Hydrogen Evolution Reaction through the Synergic Effect of N Dopants and S Vacancies. *ACS Energy Lett.* **2017**, *2*, 1022–1028. [[CrossRef](#)]
45. Hao, J.H.; Yang, W.S.; Peng, Z.; Zhang, C.; Huang, Z.P.; Shi, W.D. A Nitrogen Doping Method for CoS Electrocatalysts with Enhanced Water Oxidation Performance. *ACS Catal.* **2017**, *7*, 4214–4220. [[CrossRef](#)]
46. Yang, L.J.; Zhang, A.; Zhang, L. Light-Driven Fuel Cell with a 2D/3D Hierarchical CuS@MnS Z-Scheme Catalyst for H₂O₂ Generation. *ACS Appl. Mater. Interfaces* **2023**, *15*, 18951–18961. [[CrossRef](#)] [[PubMed](#)]
47. Biesinger, M.C.; Lau, L.W.M.; Gerson, A.R.; Smart, R.S.C. The role of the Auger parameter in XPS studies of nickel metal, halides and oxides. *Phys. Chem. Chem. Phys.* **2012**, *14*, 2434–2442. [[CrossRef](#)] [[PubMed](#)]
48. Brandt, T.G.; Tuokkola, A.R.; Yu, M.J.; Laine, R.M. Liquid-feed flame spray pyrolysis enabled synthesis of Co- and Cr-free, high-entropy spinel oxides as Li-ion anodes. *Chem. Eng. J.* **2023**, *474*, 145495. [[CrossRef](#)]
49. Kowalik, M.; Zalecki, R.; Kolodziejczyk, A. Electronic States of Colossal Magnetoresistive Manganites La_{0.67}Pb_{0.33}Mn_{1-X}Fe_XO₃ from Photoemission Spectroscopy. *Acta Phys. Pol. A* **2010**, *117*, 277–280. [[CrossRef](#)]
50. Guan, B.L.; Sheng, L.; Zhang, N.; Sun, T.; Zhu, Y.R.; Zhang, J.H.; Yi, T.F. Bimetallic metal-organic framework derived transition metal sulfide microspheres as high-performance lithium/sodium storage materials. *Chem. Eng. J.* **2022**, *446*, 137154. [[CrossRef](#)]
51. Cheng, A.; Hu, Y.N.; Yue, M.; Fu, J.X.; Wu, H.M.; Wang, S.Q.; Liu, J.W. Hollow N,C-co-doped carbon-coated ZnS nanospheres derived from metal organic framework (ZIF-8) with improved lithium and sodium storage performance. *J. Phys. Mater.* **2021**, *4*, 044003. [[CrossRef](#)]
52. Chen, Y.; Liu, H.B.; Guo, X.L.; Zhu, S.P.; Zhao, Y.; Iikubo, S.; Ma, T.L. Bimetallic Sulfide SnS/FeS Nanosheets as High-Performance Anode Materials for Sodium-Ion Batteries. *ACS Appl. Mater. Interfaces* **2021**, *13*, 39248–39256. [[CrossRef](#)] [[PubMed](#)]

53. Fu, L.K.; Kang, C.X.; Xiong, W.Q.; Tian, P.F.; Cao, S.Y.; Wan, S.Y.; Chen, H.Y.; Zhou, C.B.; Liu, Q.M. WS nanosheets@ZIF-67-derived N-doped carbon composite as sodium ion battery anode with superior rate capability. *J. Colloid Interfaces Sci.* **2021**, *595*, 59–68. [[CrossRef](#)] [[PubMed](#)]
54. Zhang, L.F.; Hu, Y.; Liu, Y.; Bai, J.X.; Ruan, H.; Guo, S.W. Tunable CuS nanocables with hierarchical nanosheet-assembly for ultrafast and long-cycle life sodium-ion storage. *Ceram. Int.* **2021**, *47*, 14138–14145. [[CrossRef](#)]
55. Zhao, C.Y.; Fan, R.Z.; Dai, J.J.; Dong, Y.T.; Wu, J.; Gao, J.K.; Cai, Y.R. Cu triggered phase transitions in FeS@NS-C anode: A neglected factor affecting the electrochemical performance of sodium storage. *Appl. Surf. Sci.* **2023**, *609*, 155407. [[CrossRef](#)]

Disclaimer/Publisher’s Note: The statements, opinions and data contained in all publications are solely those of the individual author(s) and contributor(s) and not of MDPI and/or the editor(s). MDPI and/or the editor(s) disclaim responsibility for any injury to people or property resulting from any ideas, methods, instructions or products referred to in the content.